BeBeC-2020-S1

DESIGNING SHADING SCHEMES FOR MICROPHONE PHASED ARRAYS

Christopher J. Bahr and David P. Lockard
NASA Langley Research Center
Hampton, Virginia, 23681, United States

Abstract

A technique is proposed for designing sensor weightings, or array shading functions, for microphone phased arrays. The presented method attempts to maintain mathematical simplicity while maximizing array gain for a desired mainlobe beamwidth. It does so using the two-parameter optimization of a family of functions. The shading design process is described and applied to an array used recently in the NASA Langley Research Center 14- by 22-Foot Subsonic Tunnel. Several variants of the method are compared to an existing shading scheme for the array, along with a more general optimization formulation. Results are presented for both an idealized point source and experimental data from the wind tunnel test. The shading schemes are shown to improve the behavior of array operations, but have a stronger impact on visual interpretation of maps than on source level calculations. The study results show that the two-parameter optimization scheme provides favorable characteristics while maintaining implementation simplicity.

1 INTRODUCTION

In the field of array signal processing, microphone weighting, or array shading, is a common technique for altering the output of a beamforming algorithm [9]. When shading is applied to data acquired with a microphone phased array, signals from certain microphones are emphasized more than others in subsequent data processing.

In aeroacoustic testing, array shading can serve multiple purposes: as a form of aperture control to maintain a desired beamwidth as a function of frequency [7, 8]; to compensate for the distribution of microphones in an array pattern, when clustering of microphones might overemphasize data in a certain region of the array aperture [12]; and to mitigate the effects of coherence loss over the face of the array, where propagation through a turbulent medium decorrelates signals between microphones as a function of both frequency and microphone separation [2, 12].

There is no standard technique for designing a shading function for a given array. Simple analytic methods may be used for aperture control [5], and data-dependent methods have been successfully used to compensate for coherence loss [2]. This work follows a third method, in which a shading scheme is empirically designed through the simulated response of an array to a problem of interest, achieving a desired behavior such as fixed beamwidth [7, 8, 12, 13].

2 METHODOLOGY

2.1 Shading function definition

When shading an array of microphones, each sensor is assigned a weight value. For an array of N microphones, sensor n is given the weight w_n. While, in general, these weights can have any value, for this analysis, they are constrained to be real and $w_n \geq 0$. Additionally, the shading scheme is constrained to be axisymmetric, and the array is assumed to be planar and have a circular aperture. This means that for conventional beamforming, each microphone weight can only vary with frequency, f, and microphone distance from the array center, r_n.

One suggested form of shading method uses the product of two component functions. The first component weights microphones toward the edges of the array more than those near the center, and compensates for the tendency in broadband aeroacoustic array design to cluster microphones toward an array's center. This de-emphasizes regions of the array face which would otherwise overcontribute to the averaging process. Note that this can also be accomplished with equal aperture area array designs [14], but such patterns are more difficult to design with a fixed sensor count when the operational bandwidth is high (e.g., a full-frequency decade).

The second component progressively weights microphones toward the edges of the array less than those near the array center as frequency increases, reducing the effective array aperture to hold a desired beamwidth. It also compensates for coherence loss, as the outer microphones are usually spaced much further from other microphones than the inner ones.

The weighting function thus takes the form

$$w_n(f) = u(r_n, f)\, v(r_n, f), \tag{1}$$

where u is either unity or increases with increasing r_n, and v is either unity or decreases with increasing r_n. For a given r_n and increasing f, u may vary freely, but v should decrease.

There are multiple ways to define u and v. Analytic solutions for continuous apertures may be considered [5]. Alternatively, prescribed functions with empirically determined coefficients can be designed for different operational frequency bands [7, 8], or for the whole bandwidth of the array [12, 13]. The simplicity of this last method is appealing from an optimization and implementation standpoint, and is thus used here.

Following the cited work, since u is compensating for differences in area, it is defined as some power of r_n,

$$u(r_n, f) = r_n^{\alpha(f)}, \tag{2}$$

with $\alpha(f) \geq 0$. Many functions can satisfy the requirements for v. Sijtsma and Stoker used the complimentary error function [12]. A similar behavior can be achieved using the hyperbolic tangent or Hansen's form of the modified Bessel function [5]. Alternatively, several probability density functions take the form of a power of a variable multiplied by another function. Such

probability density functions inherently meet the above specifications for a shading function.

2.2 Optimization

The overall concept for optimizing a shading function is straightforward. Some metric of the shading function or output of the beamforming algorithm is defined as a value to minimize or maximize, under a certain set of constraints. In this case, this is done as a function of frequency. A best-fit simplification may be applied to the optimizer output, or a lookup table used for each frequency.

The first choice in the optimization process is an appropriate metric. Peak sidelobe level is one option. However, calculating the peak sidelobe requires a very fine two-dimensional grid for a beamforming map to get an accurate value, and the output is highly dependent on whether or not the extents of the beamforming map properly capture all of the array's behavior of interest. A preferable alternative is to maximize the array gain. The array gain is defined as the ratio of the signal-to-noise ratio of the array to the signal-to-noise ratio of the individual sensors. When a delay-and-sum beamformer is steered to the correct source location, the array gain is given by [9]

$$G(w) = \frac{\left| \sum_{n=1}^{N} w_n \right|^2}{\sum_{n=1}^{N} |w_n|^2}. \tag{3}$$

This metric does not require an explicit beamforming map to be computed in the optimization process. Maximizing G maximizes an array's ability to average through noise uncorrelated between microphones. In many wind tunnel tests, uncorrelated contamination is a dominant form of signal interference [3]. G has a maximum value of N when a shading scheme is constant across the array, i.e., uniform weighting.

Constraints are required to keep the optimization process from outputting a uniform weighting solution. With no a priori knowledge of the coherence loss over the array face, controlling the mainlobe width of conventional beamforming output is the most obvious and straightforward option to implement. In this work, a constant beamwidth constraint is applied. Holding the beamwidth B to a constant, B_c, for increasing frequency acts as a surrogate for coherence loss correction in that it inherently de-emphasizes microphones near the edge of the array at higher frequencies. With appropriate selection, it also de-emphasizes microphones near the core of the array at lower frequencies. B_c can be selected based on resolution requirements for a given test. Determining the beamwidth requires computing a beamforming map. However, this can be done one-dimensionally for an axisymmetric array and an on-axis point source, using a root finder to get the exact value of B. One-dimensional beamforming this way keeps computational cost to a minimum and avoids gridding dependencies.

Occasionally, optimizers can arrive at unexpected extrema. In this work, it was found that holding a 3-dB mainlobe width equality constraint could, in some circumstances, find a solution where the array response met this criterion and promptly plateaued, rather than continuing to roll off with a well-defined mainlobe. To further constrain the problem, a 10-dB inequality constraint was also applied. Here, the 10-dB beamwidth could be no more than twice the 3-dB beamwidth.

To summarize, for each frequency, the optimization problem in this work is given by

$$\begin{aligned} \max_{w} \quad & G(w) \\ \text{s.t.} \quad & B_{3\text{dB}} = B_c \\ & B_{10\text{dB}} \leq 2B_c \\ & \alpha \geq 0. \end{aligned} \tag{4}$$

3 APPLICATION

The shading design technique is applied to an array pattern recently used in the NASA Langley Research Center 14- by 22-Foot Subsonic Tunnel [10]. The array, shown in Fig. 1, is a multi-arm logarithmic spiral array [14] with 11 arms and 10 microphones per arm. The innermost ring of microphones has a radius of 2.54 cm. The outermost ring has a radius of 91.44 cm. The array is designed for nominal use from 5 kHz to 50 kHz, though lower frequency operation may be desired. Initial requirements dictated that the array be able to separate noise from individual slat brackets on the installed High-Lift Common Research Model (CRM), setting the desired 3-dB beamwidth to $B_c = 15.24$ cm for a source located 3.43 m from the array face.

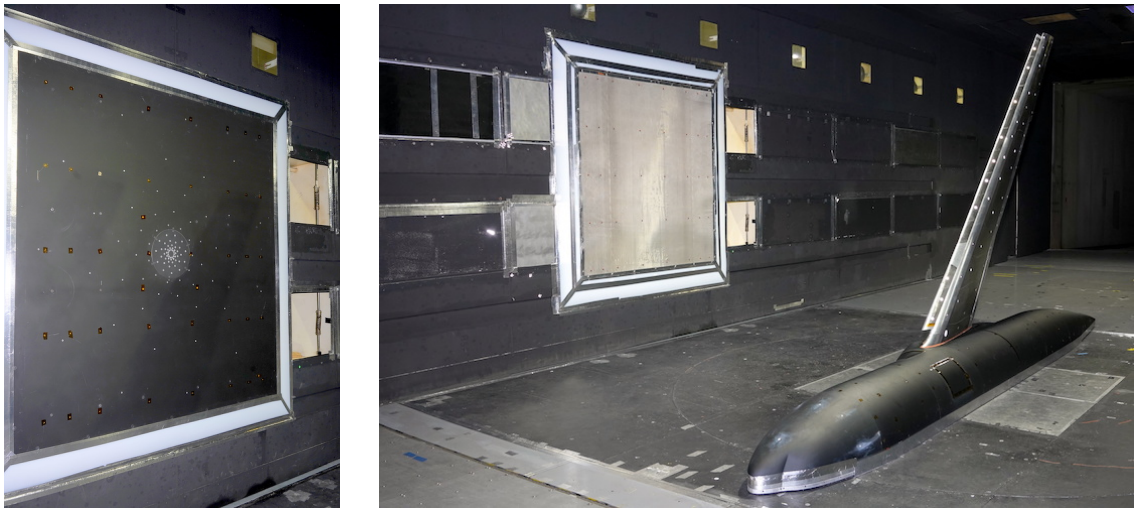

(a) *(b)*

Figure 1: Microphone array installed on the wall of the NASA Langley Research Center 14- by 22-Foot Subsonic Tunnel, shown (a) as a bare plate and (b) with a screen cover and with the High-Lift Common Research Model.

3.1 Candidate two-parameter functions

For this work, several candidate shading functions are considered. The first attempts to merge Hansen's analytic solution [5] with area compensation, and takes the form

$$w_n(f) = \rho_n^{\alpha(f)} I_0\left(\beta(f)\sqrt{1-\rho_n^2}\right), \tag{5}$$

where $\rho_n = r_n/r_{\max}$ and I_0 is the zeroth-order modified Bessel function of the first kind. The second function follows the form given by Sijtsma [12] and extended by Takaishi [13] as

$$w_n(f) = \rho_n^{\alpha(f)} \operatorname{erfc}\left(2 \times \left[\beta(f)\rho_n - 1\right]\right). \tag{6}$$

The third function follows the overall form, if not scaling, of a gamma probability density function,

$$w_n(f) = \rho_n^{\alpha(f)} e^{-\beta(f)\rho_n}. \tag{7}$$

For all of these weighting functions, an additional constraint is applied in the optimization process, $\beta \geq 0$. The parameters are optimized at 4,465 Hz and every 100 Hz from 4.5 kHz to 50 kHz, with linear interpolation applied to exact frequency values as needed.

3.2 Additional shading comparisons

The candidate two-parameter shading functions are compared with three other shading methods. The first and most simple is the baseline condition of uniform shading, or no shading at all. Here, all microphones are weighted equally.

The second shading function is one which has been used previously [10], and is based on the hyperbolic tangent function. For this array and $\rho_n > 0.3$, it takes the form

$$w_n(f) = 1 - \frac{1}{2}\left\{1 + \tanh\left[5\left(\frac{f\rho_n}{4000} - 1\right)\right]\right\}. \tag{8}$$

When $\rho_n < 0.3$, this is modified as

$$w_n(f) = \left(1 - \frac{1}{2}\left\{1 + \tanh\left[5\left(\frac{f\rho_n}{4000} - 1\right)\right]\right\}\right) \times \left\{\operatorname{sech}\left[12000\left(\frac{\rho_n - 0.3}{f}\right)\right]\right\}^7. \tag{9}$$

The coefficients in Eq. (8) and Eq. (9) were manually optimized by visually inspecting the beamforming maps after CLEAN-based deconvolution [6]. Experimental data from airframe noise measurements made of the High-Lift CRM were used, and an emphasis was placed on controlling decorrelation effects.

Finally, a more general optimization is computed. Here, no analytic functions are used. Instead, the weighting value of each ring of microphones is allowed to vary between zero and unity. The optimization is still conducted to maximize array gain for the given beamwidth constraints. However, an additional constraint is applied where the ring weight must increase monotonically with radius to a maximum at some ring, and then decrease monotonically for further increasing radius. There is no constraint on which ring has the maximum value. Note

that this generalized optimization is not intended to show the best way to compute such a shading function. Rather, it is simply an attempt to assess overall variability in array analysis when a more general shading method is applied.

4 RESULTS

4.1 Simulated performance

Results for the various shading methods are shown in Fig. 2. All optimizations were computed using the fmincon function from the MATLAB Optimization Toolbox, with the default interior-point iterative solver. Note that there is no expectation of finding a global maximum for the objective function for any of these methods. The two-parameter function families showed their convergence to be robust to the initial condition of the optimization. The same was not true for the general optimization, which showed significant variation depending on starting point. This suggests that a serious general optimization procedure would require a different problem formulation. However, the process was stable enough to meet the beamwidth constraints and include in this comparison as a first attempt. For this evaluation, the general optimization used the uniform shading function as a starting point for each frequency. Some frequencies did not return a converged optimum solution. For these, the shading function was linearly interpolated in frequency between converged solutions.

The array gain is plotted as a function of frequency in Fig. 2a. By definition, uniform shading maintains the maximum possible array gain of $N = 110$. The tanh formulation of Eqs. (8) and (9), for this frequency range, has the lowest gain. The three two-parameter functions all show similar behavior, with the erfc formulation of Eq. (6) showing slightly better low frequency performance and slightly worse high frequency performance. The gamma-pdf-based formulation of Eq. (7) shows the opposite of the erfc performance trend, while the modified Bessel function formulation of Eq. (5) falls between the two. As might be expected, the generalized optimization shows the best gain behavior of any nonuniform shading method. However, several irregularities are present on the gain versus frequency curve, which hint at the issues present with the current formulation.

The 3-dB beamwidth of the array for various shading functions is plotted in Fig. 2b. The uniform shading scheme shows the expected behavior for an array, with beamwidth reducing as frequency increases. It has the desired array beamwidth at 8.68 kHz. The tanh formulation shows the largest beamwidth, while all optimized methods meet the beamwidth constraint. The 10-dB beamwidth, shown in Fig. 2c, shows similar behavior though the 10-dB beamwidth of uniform shading far surpasses the other methods. For the optimized schemes, the 10-dB beamwidth, for the most part, holds equal to twice the 3-dB beamwidth of the array. At very low and very high frequencies, it may be slightly more narrow due to the allowable inequality, but this difference between methods is negligible for all practical purposes.

Figure 2d shows the peak relative sidelobe level for a characteristic scan plane spanning $\pm$ 2 m from the simulated on-axis point source. The uniform shading scheme holds a near-constant peak sidelobe level for the frequency range of interest, slightly increasing at higher frequencies. The tanh scheme shows the lowest sidelobe levels below about 28 kHz and sidelobe levels comparable to the optimized schemes above 28 kHz. All of the optimized methods show similar sidelobe level behavior for the full bandwidth of interest, with the three two-parameter

formulations being nearly identical. For a constant-geometry array, the peak sidelobe level appears largely insensitive to array gain with varying shading, though details of the beam pattern may change significantly.

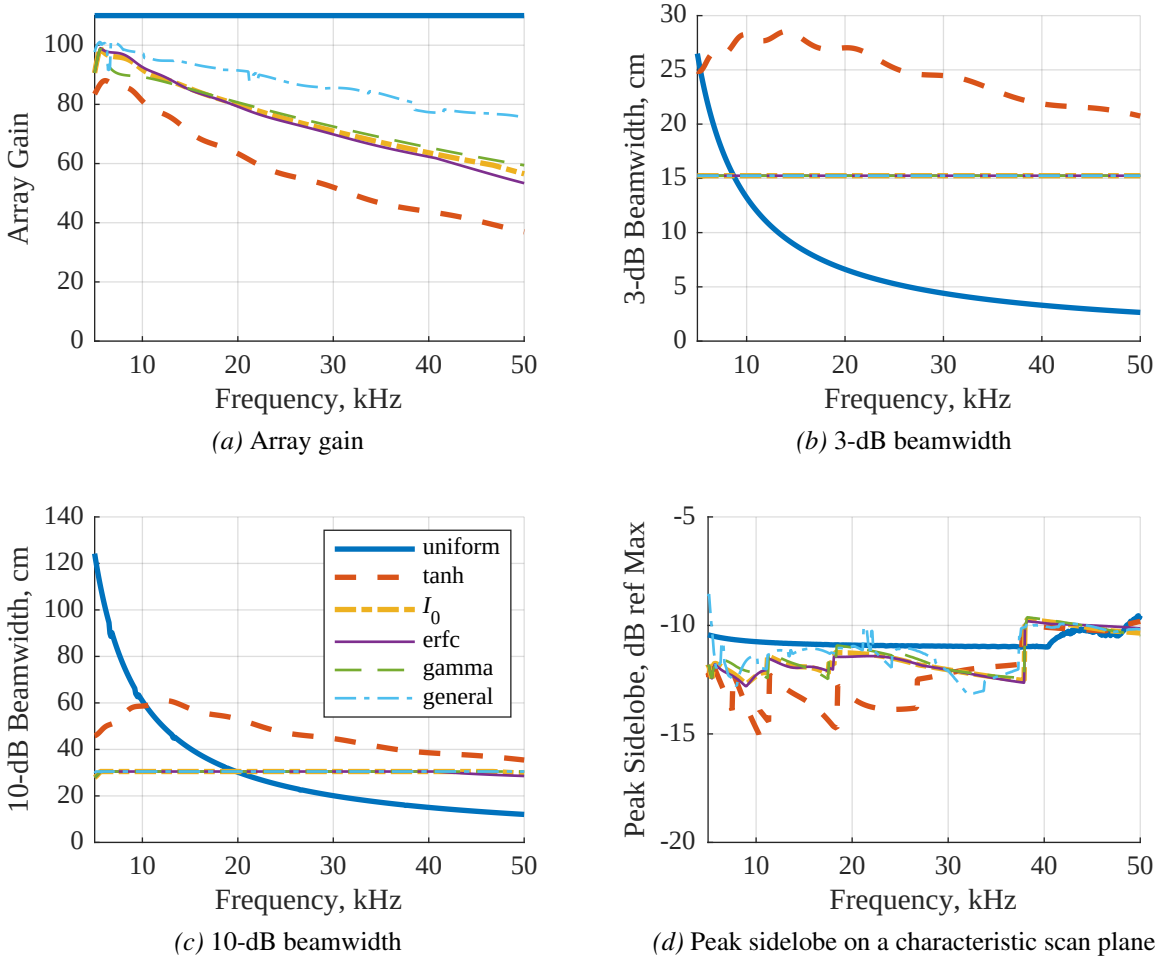

(a) Array gain

(b) 3-dB beamwidth

(c) 10-dB beamwidth

(d) Peak sidelobe on a characteristic scan plane

Figure 2: Output of optimization for the three considered functions and other shading methods.

In Fig. 3, the shading functions are shown for several different frequencies logarithmically spaced to span the 5 kHz to 50 kHz design range of the optimized methods. Markers indicate the discrete radii of rings of microphones, which are plotted logarithmically to balance ring spacing. The weight values are normalized such that $w_n^* = w_n / w_{n,\max}$. As shown in Fig. 3a, the two-parameter shading functions are effectively identical at 5 kHz, agreeing with the optimizer outputs shown in Fig. 2. The general optimization shows the same overall behavior, but with a flatter inner microphone weighting. The tanh formulation shows the same inner ring behavior as the two-parameter methods, but emphasizes midrange microphones more than the outer ring.

Figure 3b shows similar behavior between the modified Bessel and erfc formulations, while the gamma-pdf shows a sharper low-radius increase and more gradual high-radius roll-off. The generalized optimization maintains more emphasis on inner microphones and slightly less on the outer ring. The tanh formulation is progressively reducing emphasis on outer microphones,

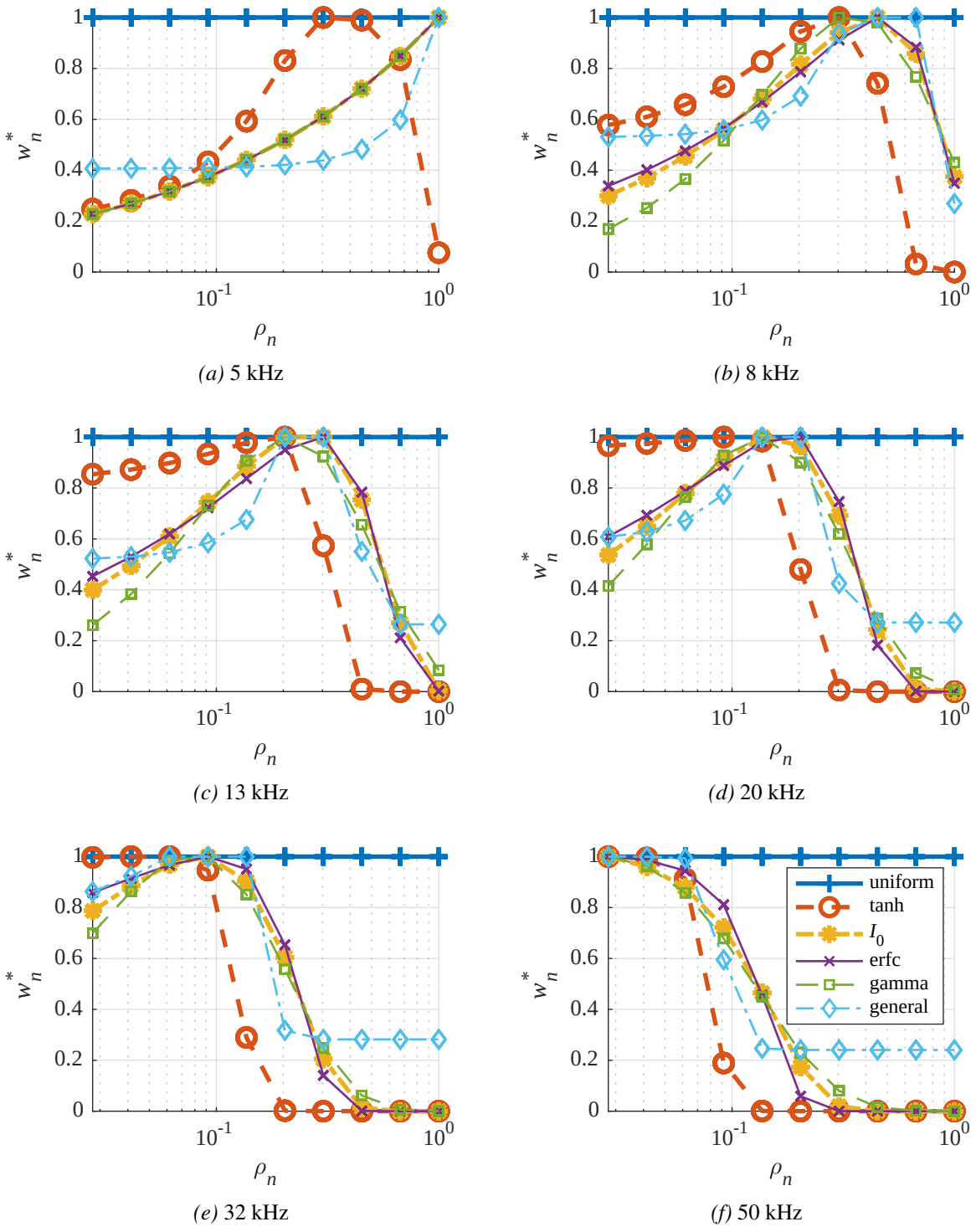

(a) 5 kHz *(b)* 8 kHz

(c) 13 kHz *(d)* 20 kHz

(e) 32 kHz *(f)* 50 kHz

Figure 3: Microphone weighting values as a function of normalized radius for varying shading schemes and frequencies of interest.

and more strongly emphasizes the inner microphones than the other methods.

The remaining frequencies shown in Figs. 3c through 3f show an increasing emphasis on the inner microphones as frequency increases. The overall behavior of the two-parameter functions is similar, with the innermost microphones emphasized by 50 kHz. The details for the roll-off regions differ slightly. The erfc method has the sharpest cutoff from a given peak, while the gamma-pdf has the most gradual. This is in agreement with the gains shown in Fig. 2a, as the more gradual roll-off maintains more of the microphone data.

From an averaging perspective this reduced roll-off is good. However, if coherence loss is a concern, the more gradual roll-off of the gamma-pdf method may preserve too much data from outer microphones. This is a benefit of the custom tanh function, which provides the best outer microphone rejection at the cost of array gain and beamwidth. The generalized optimization does the opposite. If the intent of de-emphasizing outer microphones for increasing frequency is to reduce coherence loss, the generalized method fails here by including outer microphone data at high frequencies.

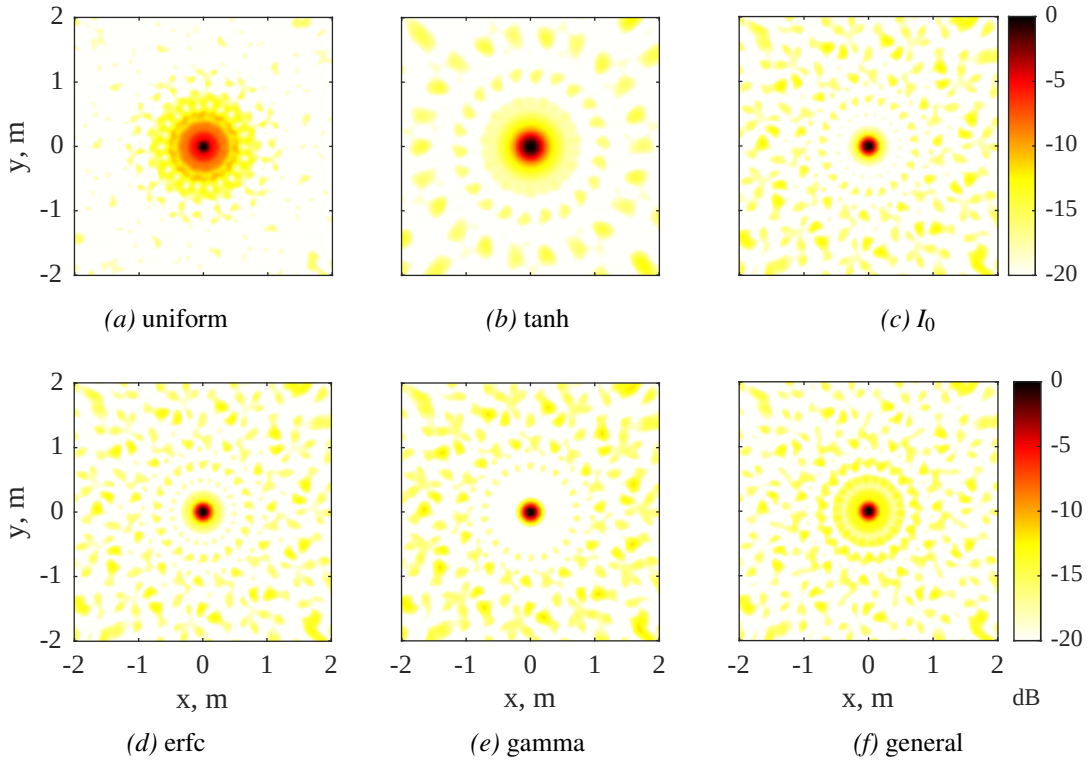

Figure 4: Sample beam maps at 8 kHz.

Beam maps at a subset of frequencies from Fig. 3 are shown in Figs. 4 through 6. The maps span ±2 m in the x- and y-directions with a grid spacing of 1 cm, and are 3.43 m from the array face.

Fig. 4 shows the results for the shading schemes at 8 kHz. Mainlobe characteristics vary between functions. Uniform shading has an extremely wide lobe between -3 db and -10 dB. This wide mainlobe structure is visible to a lesser extent on the 20 dB plot range for both the

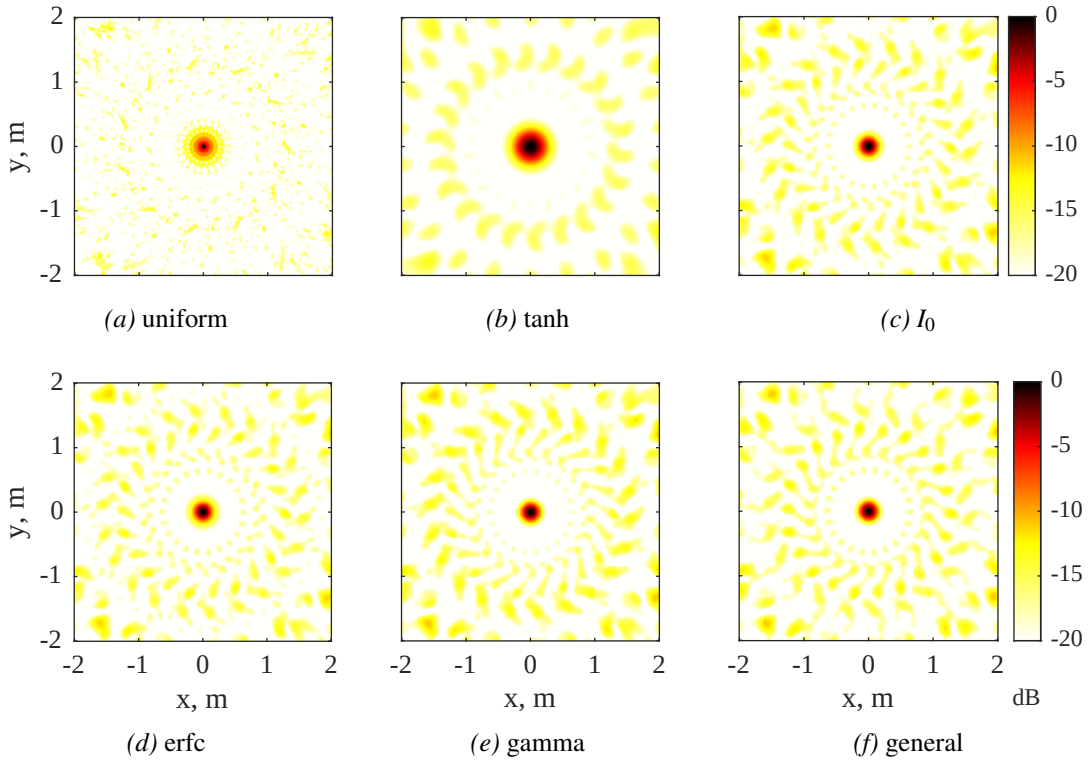

Figure 5: Sample beam maps at 20 kHz.

tanh and general shading schemes, which can be expected due to their stronger emphasis on inner microphones in Fig. 3b. The three two-parameter functions show the -20 dB mainlobe width progressively decreasing as the inner microphones are de-emphasized going from the erfc to gamma formulations. Aside from this, details of the sidelobes change but the overall behavior is similar.

The 20 kHz beam maps are shown in Fig. 5. As expected from previous plots, the mainlobe of the uniform shading scheme is much smaller than the others, while that of the tanh scheme is larger. Aside from minor details in sidelobe structure and -20 dB mainlobe width, all of the optimized shading schemes appear similar.

The 50 kHz beam maps shown in Fig. 6 continue this progression. The uniform shading scheme now has a main lobe which is barely visible on the plot scale. The tanh continues to have a wider mainlobe, and now has slightly broader sidelobes with higher levels than the optimized schemes. The optimized methods appear very similar, though the general shading scheme has a much lower inner ring of sidelobes when compared to the two-parameter family.

4.2 Experimental application

The various shading methods are now applied to experimental data acquired in the CRM aeroacoustic test. For this work, only data acquired using the array's screen cover are processed. This screen cover, consisting of a fine screen mesh overlaying a perforate steel sheet, offset the facility wall boundary layer from the array microphones and significantly improved the signal-

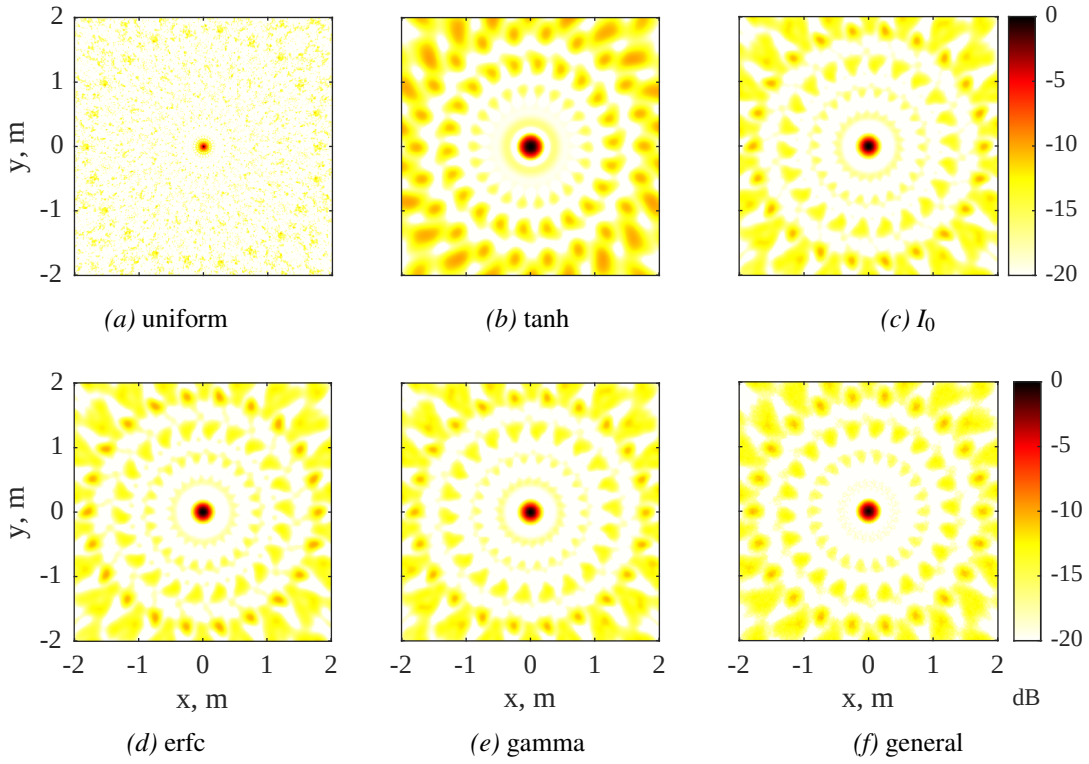

Figure 6: Sample beam maps at 50 kHz.

to-noise ratio of the measurements. The transmission loss of this cover is not corrected for in the following results, but other work suggests that, at worst, it might require a correction of 0.5 dB for the frequency range of interest.

Data were acquired at a sampling rate of 196,608 samples/sec for 35 seconds. To average through nonacoustic pressure fluctuations measured by the microphones, a relatively short block length of 2048 samples is used, yielding a narrowband binwidth of 96 Hz. The data are processed using a Hann window and 75% overlap, yielding an effective block count of 6987.

Conventional beamforming and the Deconvolution Approach for the Mapping of Acoustic Sources (DAMAS) [1] are applied to the cross-spectral matrices generated with these parameters, after applying the diagonal optimization technique described by Hald [4] to the data. Conventional beamforming results are computed using the fourth steering vector formulation addressed by Sarradj [11] with a grid spacing of 3 cm over a scan plane of 3.99 m in the x-direction and 3.48 m in the y-direction. DAMAS is applied using 200 forward-backward iterations following four different grid traversing orders. To further mitigate non-acoustic contamination, the beamforming and deconvolution maps are subsequently summed into $1/12^{\text{th}}$ octave bands prior to plotting in a model-based coordinate system independent of angle of attack.

Spectral levels as a function of frequency are computed for both discrete grid points and integrated deconvolution regions. These are left as narrowband results when plotted. The 2 kHz to 20 kHz plot range covers frequencies below the optimized range of 5 kHz to 50 kHz. Here, the array geometry cannot support the desired beamwidth. For these frequencies, the shading computed for the lowest feasible frequency, 4465 Hz, is used.

As this study is being conducted to evaluate shading functions and not airframe noise, only one test case is processed and considered. For this test case, the model has its baseline airframe configuration with a nacelle, and is set to an angle of attack of 7 degrees with a test section flow speed of Mach 0.2. An in-model speaker is active, outputting a band-limited white noise signal between 5 kHz and 10 kHz. The speaker signal provides validation of the shading scheme beam map comparisons shown in the previous section, while an example airframe noise analysis is possible with the higher frequency data in the measurement.

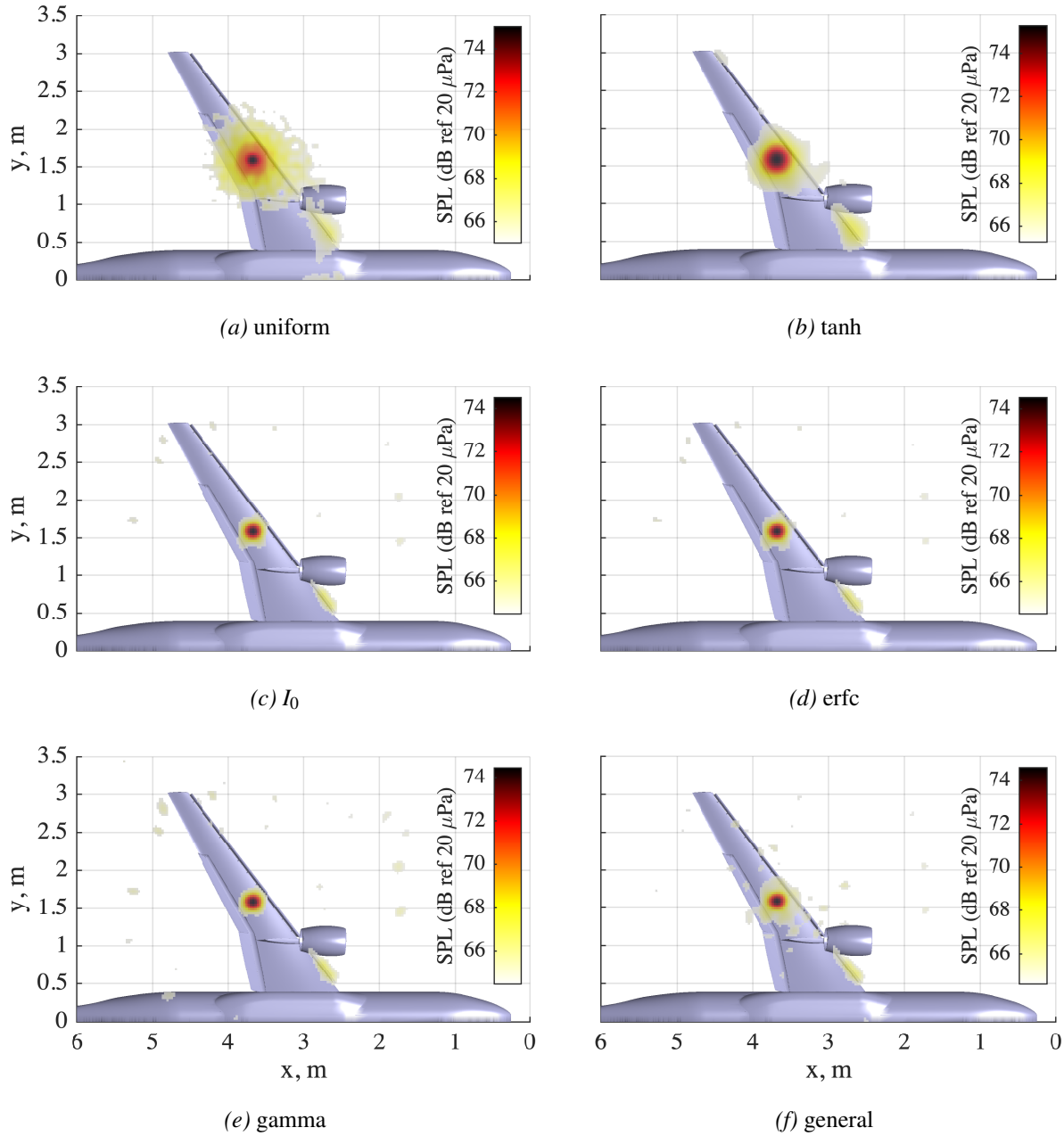

(a) uniform *(b)* tanh

(c) I_0 *(d)* erfc

(e) gamma *(f)* general

Figure 7: Sample experiment beam maps for the 8 kHz 1/12th octave band.

The speaker results at 8 kHz are shown in Fig. 7. This frequency is chosen as it allows for a direct comparison with the simulated results in Fig. 4, though these experimental results are shown on a 10-dB scale relative to their respective maximum values. As expected, all of the beamforming maps correctly localize the speaker source. They all also find an aeroacoustic source on the inboard slat. The uniform, tanh, and general methods all have broader structures around the speaker, corresponding to the wider mainlobes they showed in the -10 dB to -20 dB range in the simulated analysis. The four optimized methods all have low level sidelobes present in their maps far from the acoustic sources, with the strongest sidelobes in the gamma shading map.

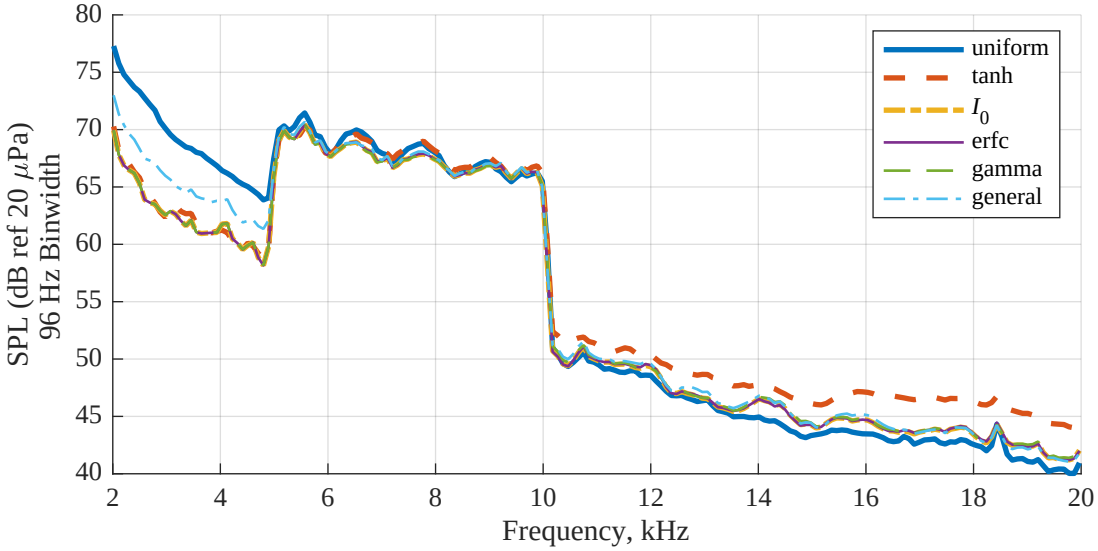

Figure 8: Beamforming map value at the speaker location as a function of frequency.

The beamforming output level for the grid point at the speaker location is shown in Fig. 8. From 5 kHz to 10 kHz, this plot shows the variability in array output for the speaker as a function of shading scheme. All of the optimized methods agree within extremely tight bounds. The uniform shading begins slightly higher in level at 5 kHz, but matches the other methods by 10 kHz. The tanh scheme tends to be bounded by the optimized methods and uniform shading, though it is the highest by 10 kHz. The overall spread of results is just over 1.5 dB at 5 kHz and just under 1 dB at 10 kHz. Whether this spread is directly due to the difference in shading functions or due to the influence of test section reverberance patterns across the array face is unknown.

At other frequencies, this plot shows the variability in array output for a region where no source should be present. For the entire range of the plot, the two-parameter optimized functions are in complete agreement. The general optimization is higher at low frequencies, approaching the other optimized methods by 20 kHz. The tanh and uniform methods swap behavior with increasing frequency. At low frequencies, tanh approximately matches the two-parameter optimizations while uniform has the highest level. At higher frequencies the uniform shading scheme shows the lowest level while tanh shows the highest. This behavior is driven by an interplay of the array's mainlobe and sidelobes contaminating the steering location output due to real acoustic sources, along with the array gain's ability to average through noise contamination.

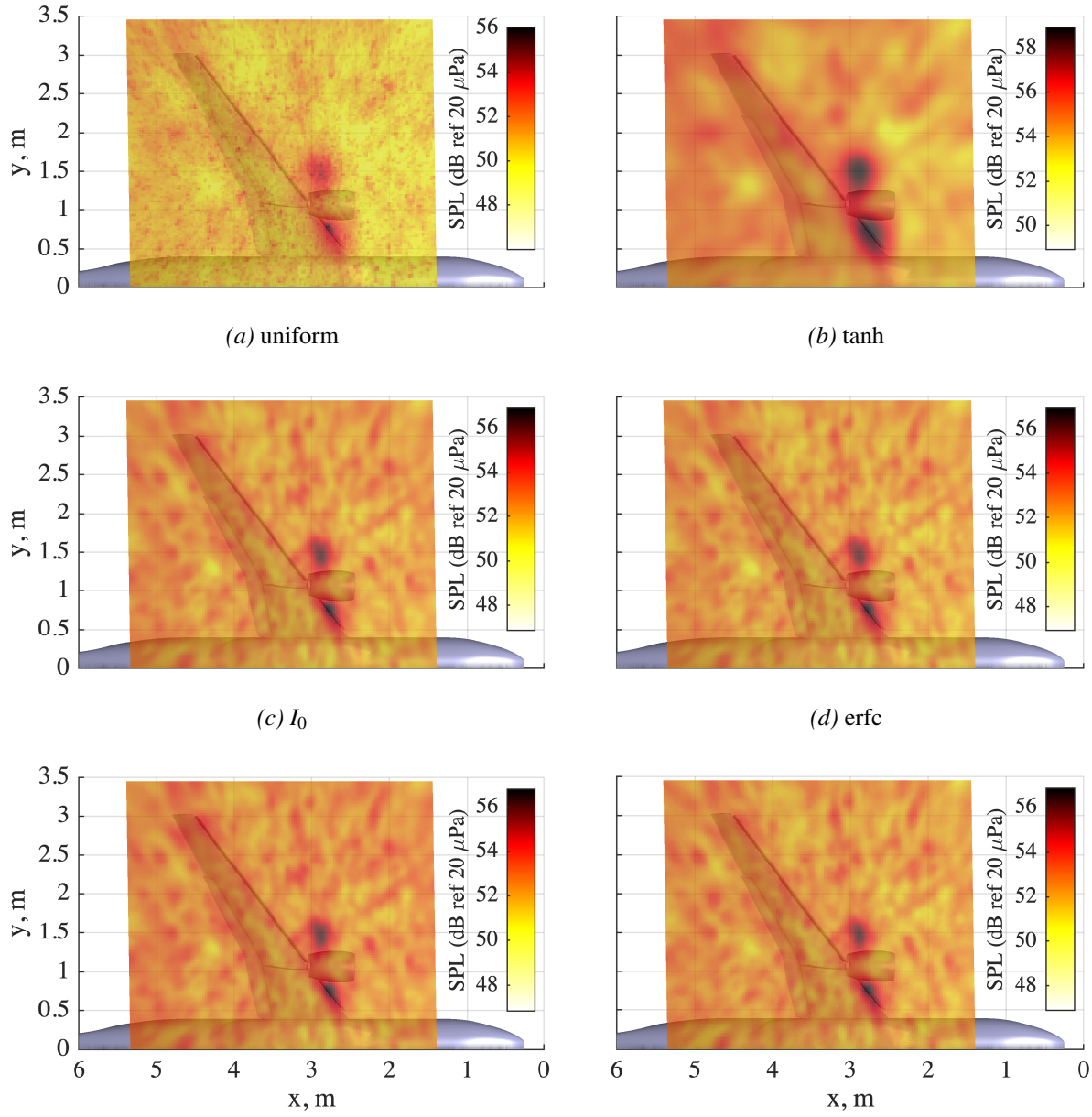

(a) uniform

(b) tanh

(c) I_0

(d) erfc

(e) gamma

(f) general

Figure 9: Sample experiment beam maps for the 20 kHz 1/12th octave band.

The test results at 20 kHz are shown in Fig. 9. Here, two sources are evident in the data. The strongest airframe noise source is located on the inboard slat, below the nacelle. An additional source is visible above the nacelle. Separate investigation suggests this is a reflection coming from the far wall of the wind tunnel test section, possibly originating from a strong source on the suction side of the model. The overall behaviors of the shading schemes are similar for this frequency. The uniform scheme, with the smallest beamwidth, has the tightest localization of both major sources. It also shows slightly lower background levels in the beam map. The tanh

method clearly has the widest beamwidth here, and also tends to emphasize the reflected source the most. It shows peak beamforming levels more than 2 dB higher than the other shading schemes. All four optimized methods appear extremely similar in their map details.

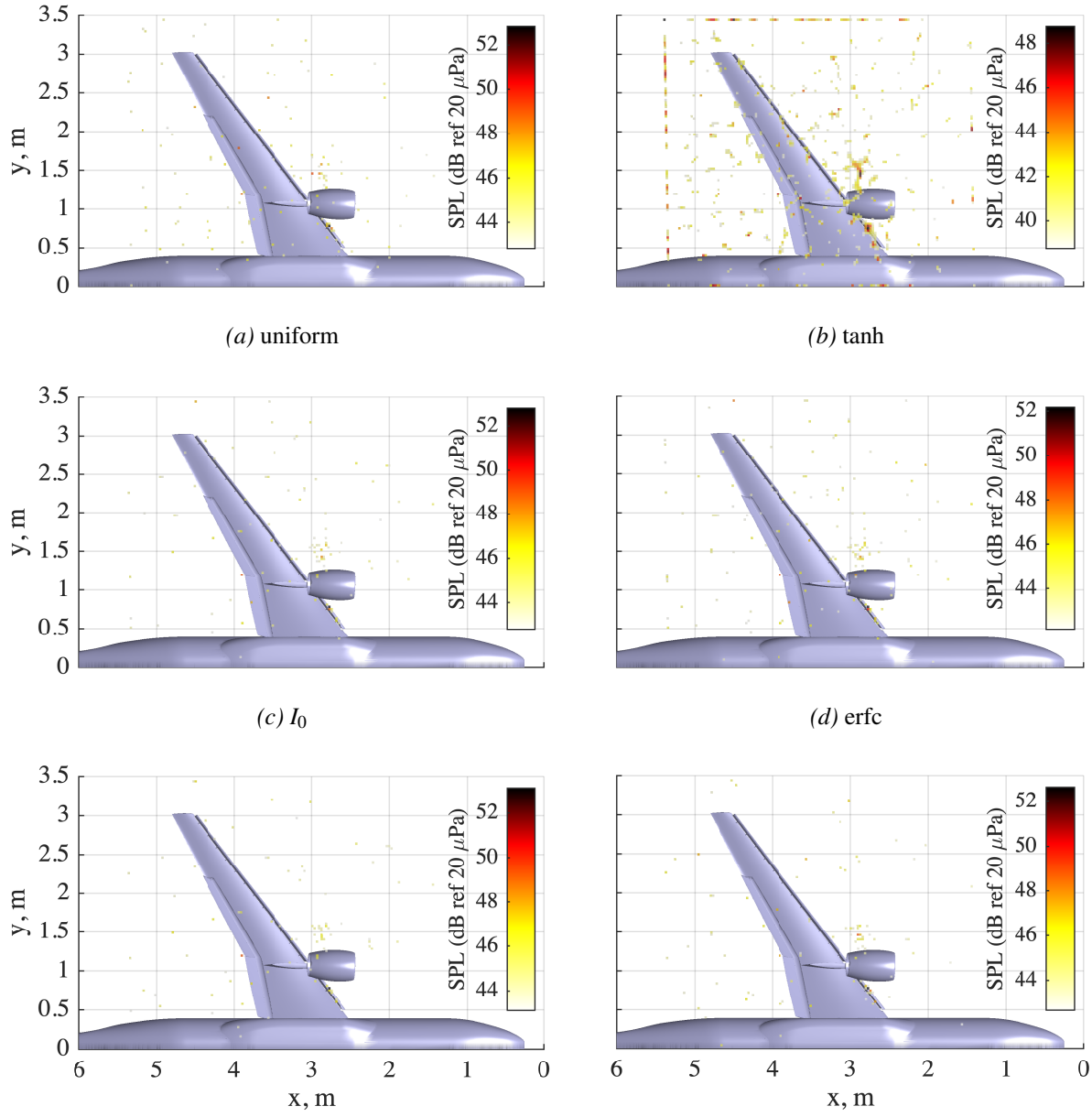

(a) uniform *(b)* tanh

(c) I_0 *(d)* erfc

(e) gamma *(f)* general

Figure 10: Sample experiment DAMAS output for the 20 kHz 1/12th octave band.

The deconvolution results of the beam maps in Fig. 9 are shown in Fig. 10. Five of the six shading schemes are broadly similar. For the most part, the uniform and all optimized methods locate the same sources to similar levels, though they distribute them slightly differently. The general optimization appears to have qualitatively fewer spurious deconvolution artifacts,

though they could still be present just under the 10 dB plot scale. Uniform shading appears to have slightly more artifacts.

The one exception to similarity is the nonoptimized tanh method. This tends to show source smearing. It also drives a significant amount of energy to the boundaries of the deconvolution grid. The strongest source in the tanh deconvolution is actually on the boundary. The color map had to be shifted downward by over 4 dB to have a peak level corresponding to the model acoustic sources. This behavior is suspected to be due to the grid resolution versus beamwidth of the processed array response. However, sensitivity to contamination due to reduced array gain or some other effect may also influence it.

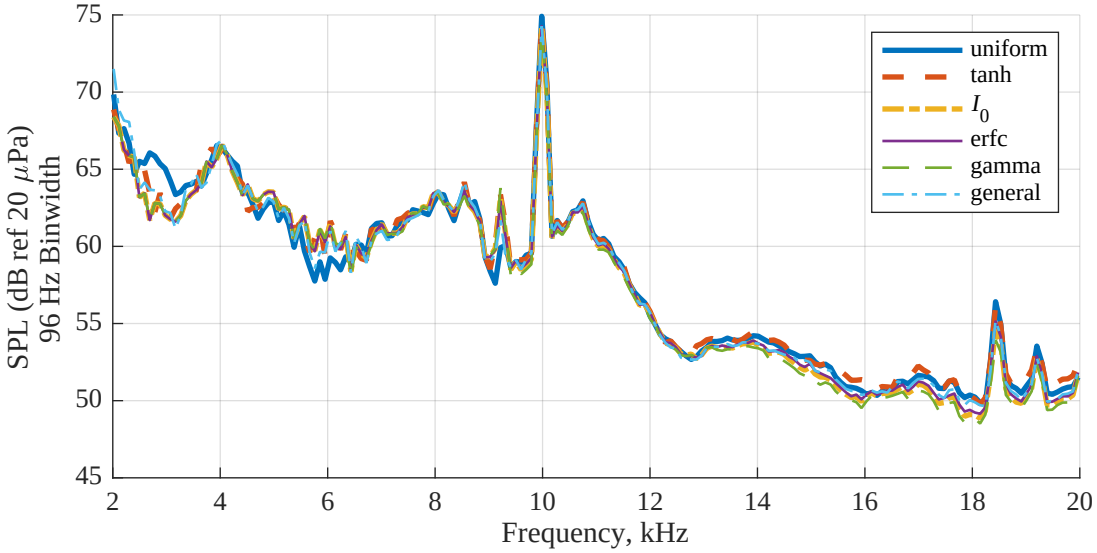

Figure 11: Integrated spectra for the inboard slat region of the DAMAS results.

To evaluate the influence of shading schemes on total calculated acoustic levels, the integrated level of the inboard slat and nacelle pylon interaction region is shown in Fig. 11. This is calculated by summing the narrowband DAMAS results in the region of 2.5 m $\leq x \leq$ 3 m and 0.5 m $\leq y \leq$ 1 m. For the most part, the results are similar and capture the same spectral shape. Uniform shading shows some deviation at lower frequencies where every other shading scheme is in approximate agreement. All of the methods appear to capture the peak at 10 kHz as the same level. At high frequencies, uniform and tanh shading schemes show slightly higher level estimates than the optimized methods. All of the optimized methods are within a fraction of a dB of each other above 3 kHz.

5 SUMMARY AND CONCLUSIONS

A shading function optimization method is presented, intended to calculate weighting values for broadband microphone phased arrays. The shading function is assumed to have a form of the product of two component functions, one which monotonically increases and one which monotonically decreases with microphone radius. Optimization is performed to maximize the array gain for a delay-and-sum beamformer, under the equality constraint of a constant 3-dB

beamwidth and an inequality constraint on the 10-dB beamwidth. These two-parameter formulations are compared with an existing shading scheme for an example array used in a recent wind tunnel test, along with a more general optimization scheme.

Initial results show similar behavior among the optimized functions. The general optimization maintains a higher array gain than the two-parameter family of functions, at the expense of including outer array microphones at frequencies where they may experience decorrelation problems. The optimized methods all have an array gain greater than the existing shading method. Sidelobes appear insensitive to which function is optimized.

Visually, the optimization results provide favorable characteristics in both simulated and experimental beam maps. Sources are well-localized, and the aperture control of the constant beamwidth constraint avoids some source smearing at lower frequencies. Deconvolution results show that, for the most part, DAMAS is insensitive to shading scheme selection, though the behavior of the tanh results may suggest the importance of selecting a reasonable number of points per beamwidth.

Quantitatively, both beamforming and deconvolution are affected by shading scheme selection, but do not appear significantly influenced by the fine details of each method. All of the optimized techniques behave nearly identically in tracking the peak level of the speaker source and in determining the integrated level of the inboard slat. These optimized methods differ from uniform shading and from the custom tanh scheme, though are generally in agreement with each other.

Overall, it appears that having a shading scheme is important, and maintaining a constant beamwidth as a function of frequency while maximizing array gain is a means to generate weights that exhibit desirable beamforming behavior. The considered two-parameter family of functions is well-behaved in the optimization process, and practically loses little when compared to the general optimization. The current formulation for a general optimization does not appear worth the extra effort to implement, though a more well-constrained version might be worth considering in the future. The specific function selection of the two-parameter family appears to be in general a matter of preference, trading off between maximizing array gain and maximizing rejection of outer microphones at higher frequencies.

6 ACKNOWLEDGMENTS

The authors would like to acknowledge the support provided by the 14- by 22-Foot Subsonic Tunnel team, and by colleagues in the Aeroacoustics, Structural Acoustics, and Advanced Measurement and Data Systems branches at the NASA Langley Research Center. In particular, they wish to thank Mr. Lawrence E. Becker, Mr. William M. Humphreys, Jr., and Mr. Daniel J. Stead for their work in the setup, debugging, and data acquisition for the acoustic portion of the CRM test.

References

[1] T. F. Brooks and W. M. Humphreys. “A deconvolution approach for the mapping of acoustic sources (DAMAS) determined from phased microphone arrays.” *J. Sound Vib.*, 294, 856–879, 2006.

[2] F. R. do Amaral, F. H. T. Himeno, C. C. Pagani, Jr., and M. A. F. de Medeiros. "Slat noise from an MD30P30N airfoil at extreme angles of attack." *AIAA J.*, 56(3), 964 – 978, 2018.

[3] R. P. Dougherty. *Aeroacoustic Measurements*, chapter 2. T. J. Mueller, ed., Springer-Verlag Berlin Heidelberg New York, 2002.

[4] J. Hald. "Removal of incoherent noise from an averaged cross-spectral matrix." *J. Acoustic. Soc. Am.*, 142(2), 846–854, 2017.

[5] R. C. Hansen. "A one-parameter circular aperture distribution with narrow beamwidth and low sidelobes." *IEEE Trans. Antennas Propag.*, 24(4), 477 – 480, 1976.

[6] J. A. Högbom. "Aperture synthesis with a non-regular distribution of interferometer baselines." *Astron. Astrophys. Suppl.*, 15, 417 – 426, 1974.

[7] W. M. Humphreys, Jr., T. F. Brooks, C. J. Bahr, T. B. Spalt, S. M. Bartram, W. G. Cullition, and L. E. Becker. "Development of a Microphone Phased Array Capability for the Langley 14- by 22-Foot Subsonic Tunnel." In *20th AIAA/CEAS Aeroacoustics Conference, AIAA Aviation 2014, Atlanta, GA*, AIAA Paper 2014-2343. 16 – 20 June, 2014.

[8] W. M. Humphreys, Jr., T. F. Brooks, W. W. Hunter, Jr., and K. R. Meadows. "Design and Use of Microphone Directional Arrays for Aeroacoustics Measurements." In *36th Aerospace Sciences Meeting & Exhibit, Reno, NV*, AIAA Paper 98-0471. 12 – 15 January, 1998.

[9] D. H. Johnson and D. E. Dudgeon. *Array Signal Processing: Concepts and Techniques*, chapter 4. Prentice Hall, Upper Saddle River, NJ, 1993.

[10] D. P. Lockard, M. D. O'Connell, V. N. Vatsa, and M. M. Choudhari. "Assessment of Aeroacoustic Simulations of the High-Lift Common Research Model." In *25th AIAA/CEAS Aeroacoustics Conference, Delft, The Netherlands*, AIAA Paper 2019-2460. 20 – 23 May, 2019.

[11] E. Sarradj. "Three-dimensional acoustic source mapping with different beamforming steering vector formulations." *Advances in Acoustics and Vibration*, 2012(292695), 1–12, 2012.

[12] P. Sijtsma and R. W. Stoker. "Determination of Absolute Contributions of Aircraft Noise Components Using Fly-over Array Measurements." In *10th AIAA/CEAS Aeroacoustics Conference , Manchester, Great Britain*, AIAA Paper 2004-2958. 10 – 12 May, 2004.

[13] T. Takaishi, H. Ura, K. Nagai, Y. Yokokawa, M. Murayama, Y. Ito, R. Sakai, H. Shoji, and K. Yamamoto. "Airframe noise measurements on JAXA jet flying test bed 'Hisho' using a phased microphone array." *Int. J. Aeroacoustics*, 16(4 – 5), 255 – 273, 2017.

[14] J. R. Underbrink. *Aeroacoustic Measurements*, chapter 3. T. J. Mueller, ed., Springer-Verlag Berlin Heidelberg New York, 2002.